

Tailoring the Angular Mismatch in MoS₂ Homobilayers through Deformation Fields

Kory Burns, Anne Marie Z. Tan, Jordan A. Hachtel, Anikeya Aditya, Nitish Baradwaj, Ankit Mishra, Thomas Linker, Aiichiro Nakano, Rajiv Kalia, Eric J. Lang, Ryan Schoell, Richard G. Hennig, Khalid Hattar, and Assel Aitkaliyeva*

Ultrathin MoS_2 has shown remarkable characteristics at the atomic scale with an immutable disorder to weak external stimuli. Ion beam modification unlocks the potential to selectively tune the size, concentration, and morphology of defects produced at the site of impact in 2D materials. Combining experiments, first-principles calculations, atomistic simulations, and transfer learning, it is shown that irradiation-induced defects can induce a rotation-dependent moiré pattern in vertically stacked homobilayers of MoS_2 by deforming the atomically thin material and exciting surface acoustic waves (SAWs). Additionally, the direct correlation between stress and lattice disorder by probing the intrinsic defects and atomic environments are demonstrated. The method introduced in this paper sheds light on how engineering defects in the lattice can be used to tailor the angular mismatch in van der Waals (vdW) solids.

K. Burns, A. M. Z. Tan, R. G. Hennig, A. Aitkaliyeva Department of Materials Science & Engineering University of Florida Gainesville, FL 32611, USA E-mail: aitkaliyeva@mse.ufl.edu K. Burns, E. J. Lang, R. Schoell, K. Hattar Center for Integrated Nanotechnologies Sandia National Laboratories

Albuquerque, NM 87545, USA K. Burns

Department of Materials Science & Engineering University of Virginia

Charlottesville, VA 22904, USA

J. A. Hachtel

Center for Nanophase Materials Science

Oak Ridge National Laboratory

Oak Ridge, TN 37830, USA

A. Aditya, N. Baradwaj, A. Mishra, T. Linker, A. Nakano, R. Kalia

Department of Physics

University of Southern California

Los Angeles, CA 90089, USA

E. J. Lang

Department of Nuclear Engineering

University of New Mexico

Albuquerque, NM 87131, USA

K. Hattar

Department of Nuclear Engineering

University of Tennessee

Knoxville, TN 37996, USA



The ORCID identification number(s) for the author(s) of this article can be found under https://doi.org/10.1002/smll.202300098.

DOI: 10.1002/smll.202300098

1. Introduction

2D materials and their heterostructures have an additional degree of freedom, that is, the ability to manipulate interlayer twist angles. For example, one can form moiré superlattices by stacking two similar layers on top of each other and engineering a small angular twist between layers.^[3] The twist angle governs the crystal symmetry, thus precise control of the interlayer twist angle of 2D materials will provide a basis for the development of twistronics for various electronic and photonic applications.[4] Extensive efforts have been made to engineer the twist angle of vdW solids utilizing a range of techniques including transfer methods, [5,6] robotic assemblies,[7] growth conditions,[8-10] and other

manipulation techniques. [11–13] It should be noted that this all starts with the ability to fabricate high-quality, large-area sheets of the vdW material of interest. [14–18] In addition, others have explored possibilities of coupling 2D materials with SAWs for increased functionalities, [19–21] as strain-induced fields excite acoustic vibrations that can interact with moving chargers. The role defects play on compressive/tensile strains of monolayer MoS_2 has also been investigated, where we found that S vacancies induce a compressive strain and Mo vacancies produce a tensile strain. [22,23] Of course, this will cause variations in lattice constants of vertically stacked sheets of similar materials, assuming one layer has a different defect concentration than the other.

The rotational mismatch between vertically stacked layers of similar materials occurs to minimize the elastic deformation energy in the system.^[24] Previously, researchers have engineered defects on the substrate and placed MoS₂ on a defected substrate to generate ripples and discontinuities on the material.^[25] Additionally, by applying mechanical loads to a thin membrane one can initiate a crack formation followed by a phase transformation.^[26–28] However, ion irradiation has gained prominence and has been used to controllably modify the surface of 2D materials with high efficiency.^[29–31] The impinging ion transfers its energy to the target material by both elastic collisions and inelastic interactions, where the damage produced on the target material occurs through energy deposition. It has been proposed that increasing the angle of incidence of the impinging ion on MoS₂ has an increasing probability to form

pores in the material,^[32] as nanopore generation is derived from atomic sputtering. Large-scale atomic sputtering is produced in response to in-plane collisional cascades,^[33] generating impactful deformation fields emanating from large defect pores.^[22] These deformation fields cause local displacements of the surrounding lattice, which should alter the periodicity of the moiré patterns in bilayer MoS₂ sheets, as previously seen in twisted bilayer graphene.^[34,35]

We, therefore, hypothesize that damage (i.e., extended defects such as nanopores) can also be used to induce moiré superlattices and provide an avenue for controlling twist angle in vdW solids. This is because damage introduces thermoelastic stresses and strains, which will deform atomically thin vdW materials and excite SAWs. To test this hypothesis, we coupled in situ ion irradiation high resolution transmission electron microscopy (HR-TEM), scanning TEM (STEM), selected-area electron diffraction (SAED), density functional theory (DFT), transfer learning, and molecular dynamics (MD) simulations and investigated the physics behind the formation of moiré patterns in MoS₂. We observe, for the first time, how engineering phase boundaries, increasing point defect concentration, and generating nanopores cause localized deformation fields in the lattice, facilitated by the formation of ripples in vdW solids, and subsequently, rotational misalignment. Our systematic investigation yields insight into a new direction for tuning the moiré potential in vdW solids and paves the way for a new methodology for accessing hidden physical phenomena in vertically stacked materials.

2. Characterization and Formation of Defects and Phase Transformations

We begin by exploring charged projectiles to generate defect structures in few-layer sheets of MoS₂. First, when selecting our ion beam parameters for processing, Monte Carlo simulations are deployed with a soft range of ions in matter (SRIM).[36] We calculated the sputtering yield of Mo and S atoms with ion energies ranging from 15 keV to 15 MeV, with light ions (He), intermediate-sized ions (Mo), and heavy ions (Au). Additionally, the angle of incidence was varied from 0° to 60°, which changes the lateral trajectory of the ion inside the target material. We provide a summary of the results in Table S1, Supporting Information. At higher angles of incidence, the defect concentration gradient (i.e., the number of sputtered atoms on the top layer relative to the bottom layer) was much higher, this is because the projectiles propagate laterally through the sheet as opposed to a head-on collision, which initials collisional cascades in the film. Also, at lower energies, the velocity of the projectile is greatly decreased, making the irradiation surface sensitive and generating more sputtering. By analyzing the number of ions studied, and the ratio of sputtering between Mo and S atoms, we design our irradiation experiment to introduce a controlled amount of localized damage on the sheets post-fabrication.

Intrinsic structural defects are present in fabrication-induced processes, which were observed abundantly in various regions in the lattice. The structural integrity of the film was assessed pre- and post-ion irradiation as probing the local atomic environment was paramount to assessing the rotational degrees of freedom in this study, which will be discussed more in a

later section. First, we introduce the atomic vacancies present during the fabrication process. See Figure S1, Supporting Information, for the description of the process used to generate STEM data presented in this manuscript. Figure 1a displays high-angle annular dark-field (HAADF) STEM view of the enumerations of intrinsic defects in few layer 2H-MoS2 found in the as-fabricated sheets. The order in which the defects are displayed is in order of increasing formation energy in S-rich conditions: $[^{22,37,38}]V_S$, $V_{S2(c)}$, $V_{S2(p)}$, V_{Mo} , V_{MoS2} , V_{MoS3} , and V_{MoS6} . The antisite defects in few layer MoS₂, shown in Figure S2, Supporting Information, are presented in order of most abundantly found: Sada-S, S2Mo, and MoS2. This can be attributed to the likely p-type carrier concentration of the starting material during synthesis, which is further supported by spectroscopy measurements displayed in Figure S3, Supporting Information. For a more detailed overview of how individual defects were characterized, refer to Figure S4, Supporting Information. After analyzing the pristine flakes, we then subjected our material to 2.8 MeV Au^{4+} ions at temperatures of -180, 25, 300, and 800 °C, a fixed fluence of 1×10^{13} cm⁻², and an angle of incidence of 60°. The influence of the temperature during ion beam irradiation was that increased temperature led to a higher defect concentration, allowing tunability of the defect morphology, concentration of defects, and surface area in which different structural phases emerged.

Figure 1b presents the structural phases of MoS2 observed throughout the experiment. The hexagonal arrangement of atoms verifies the 2H phase which dominates the surface area of the flakes, as this phase is the ground state. The Mo and S atoms are easily distinguishable with z-contrast imaging in STEM mode as they have large variances in atomic number. In bilayer MoS₂, the difference becomes more subtle due to the AA' stacking sequence with Mo and S overlaying each other with strong out-of-plane interactions (Figure S5, Supporting Information). The 3R phase (AB) seen primarily during the 300 °C irradiation has a broken inversion symmetry from its 2H phase counterpart, which it maintains from single layer to bulk configurations. The 3R phase is the most "compact" polymorph of MoS₂, electron–electron repulsion from filled nonbonding d₂²orbitals is balanced by vdW forces holding the layers together. This combination of effects results in an interlayer Mo-Mo distance of 6.13 Å with a sandwich height of 2.98 Å.[39]

The 1T-phase (AB') is thermodynamically metastable and dominated in regions of disorder from a combination of lattice strain and charge transfer inducing S atoms to glide to a lower energy atomic position under stress. With these phases being present from local atomic environments, intuitively one can imagine there are phase boundaries between the α (amorphous) and 1T phase (α | 1T). This phase transition depends on the dose of impinging particles (i.e., vacancy concentration) and thermal environments (i.e., mechanical strain). In our case, both methods were utilized. Increasing the S-dominated vacancy concentration, in which S vacancies act as electron acceptors, increases the density of electrons in the d-orbital and destabilizes the 2H phase. [40] Additionally, increased bond lengths induced by thermal stresses during the irradiation assisted in generating a larger vacancy concentration at lower doses. The α phase is generated from high Mo and S vacancy concentrations, leading to the destruction of translational perio-

www.small-iournal.com

16136829, 0, Downloaded from https://onlinelibrary.wiley.com/doi/10.1002/smll.202300098 by Oak Ridge National Laboratory, Wiley Online Library on [07/04/2023]. See the Terms and Conditions (https://onlinelibrary.wiley.com/term

and-conditions) on Wiley Online Library for rules of use; OA articles are governed by the applicable Creative Commons License

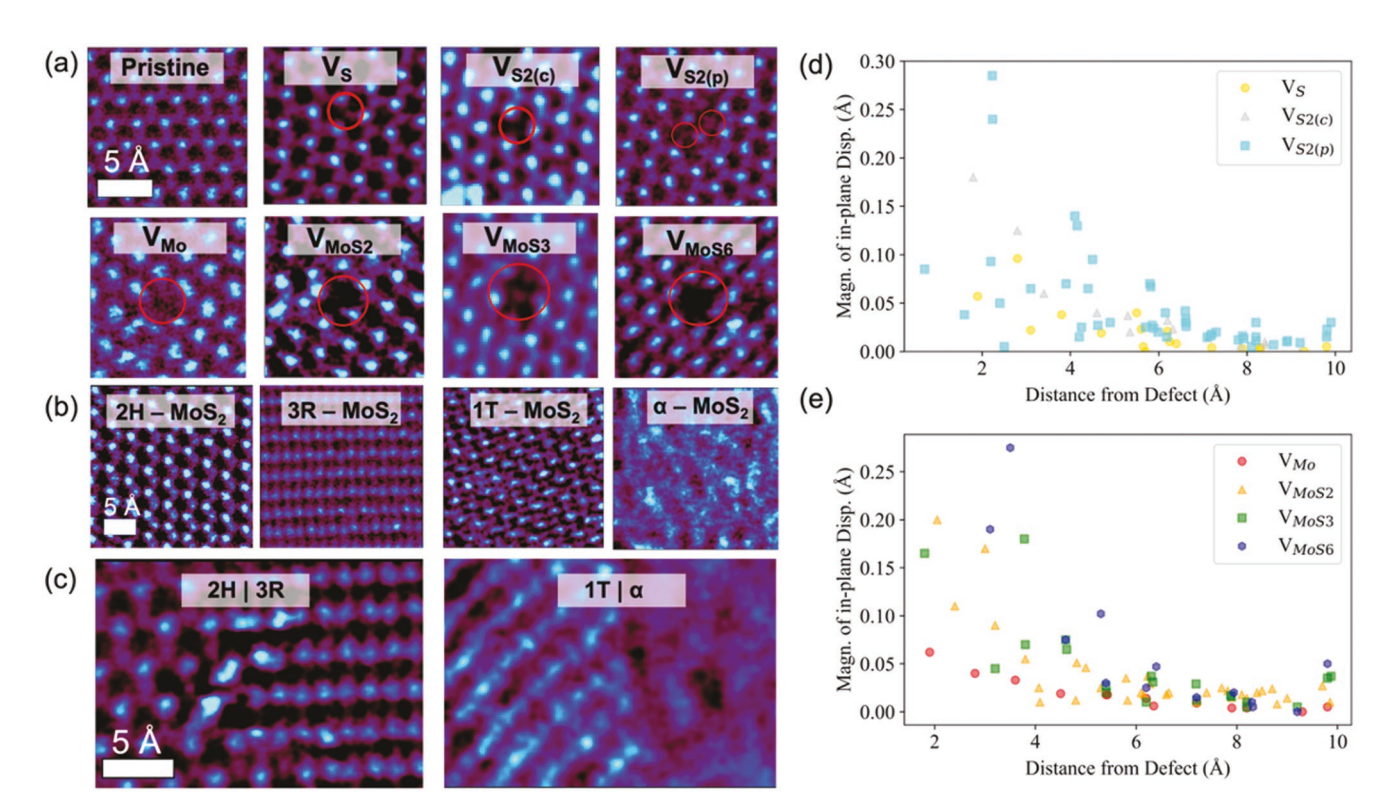


Figure 1. Atomically resolved HAADF STEM images of structural phases and fabrication-induced defects in MoS2, a) Pristine lattice of MoS2 followed by all the point defect complexes seen during fabrication processes. b) Micrographs displaying phases present throughout the lattice during our experiment. c) Micrographs showcasing commonly found phase boundaries in MoS2 through ion irradiation experiments. In-plane displacements as a function of in-plane distance from defect for d) V_S complexes, and e) V_{Mo} complexes compiled from DFT calculations.

dicity in the crystal observed during the 800 °C irradiation. At this temperature, the vacancy diffusion rate was faster than the vacancy generation rate, causing extended defects and increased surface energy in the film. These conditions caused the single layer to lose structural tacticity, but phase boundaries to the 1T phase in bilayer MoS₂ were still present (α | 1T).

Figure 1d plots the magnitudes of the in-plane displacements as a function of in-plane distance from the defect as calculated with DFT, for the V_S complexes. The isolated Sulfur vacancy (V_S) has the smallest in-plane displacement from the point of origination to 10 Å away, followed by the columnar disulfur vacancy $(V_{S2(c)})$ with two vacancies in the same column, and the planar disulfur vacancy ($V_{\rm S2(p)}$), with two vacancies neighboring each other in the top surface. Figure 1e plots the same quantity for the V_{Mo} complexes. The isolated Mo vacancy (V_{Mo}) has the smallest in-plane displacement, followed by V_{MoS2} , $V_{\text{MoS}3}$, and $V_{\text{MoS}6}$. The observed trends in the in-plane displacements reflect the complexity of the strain fields generated by different types of vacancy defects. Clearly, the strain field is non-uniform and highly influenced by the different orientations of defects—for example, $V_{S2(p)}$ generates a much larger displacement than $V_{S2(c)}$ due to the constructive overlapping of the strain fields from neighboring in-plane S vacancies. In addition, we also observe that the resultant displacements from a vacancy agglomeration are far from a linear combination of the displacements from individual vacancies. Isolated Mo and S vacancies generate tensile and compressive strains, respectively. This, combined with additional relaxations within the defects,

results in the vacancy agglomerations containing both Mo and S vacancies generating relatively smaller strain fields than a linear combination of the strain fields from the corresponding isolated vacancies. Our DFT results clearly demonstrate that the strain fields generated by different vacancy agglomerations can be rather complex and cannot be simply extrapolated from smaller agglomerations to larger agglomerations. During irradiation, we expect larger vacancy agglomerations to form, which due to size constraints, cannot be modeled within DFT. Hence, as described later in this work, a Stillinger-Weber (SW) forcefield was used to perform MD simulations of large nanopores. To further provide validation to the DFT calculations used in this work and additional clarity, we refer the reader to Figure S6, Supporting Information.

3. Characterization of Moiré Patterns in Misaligned MoS₂

The versatility of our method enables fine control over the rotational mismatch in vdW solids with an ion beam stimulus. To understand this approach, we first display how the moiré patterns originate, the realm of possible enumerations, and the method adopted to characterize the patterns. The ion beam irradiation generates a defect concentration gradient in sequentially stacked layers, causing the layers to rotate with respect to one another to minimize the elastic deformation energy between layers. Figure 2a presents two diagrams: a 0° rotational misalignment www.advancedsciencenews.com

16138289, 0, Downloaded from https://onlinelibrary.wiley.com/doi/10.1002/smll.202300098 by Oak Ridge National Laboratory, Wiley Online Library on [07/04/2023]. See the Terms and Conditions (https://onlinelibrary.wiley.com/terms-and-conditions) on Wiley Online Library for rules of use; OA articles are governed by the applicable Creative Commons Licenses

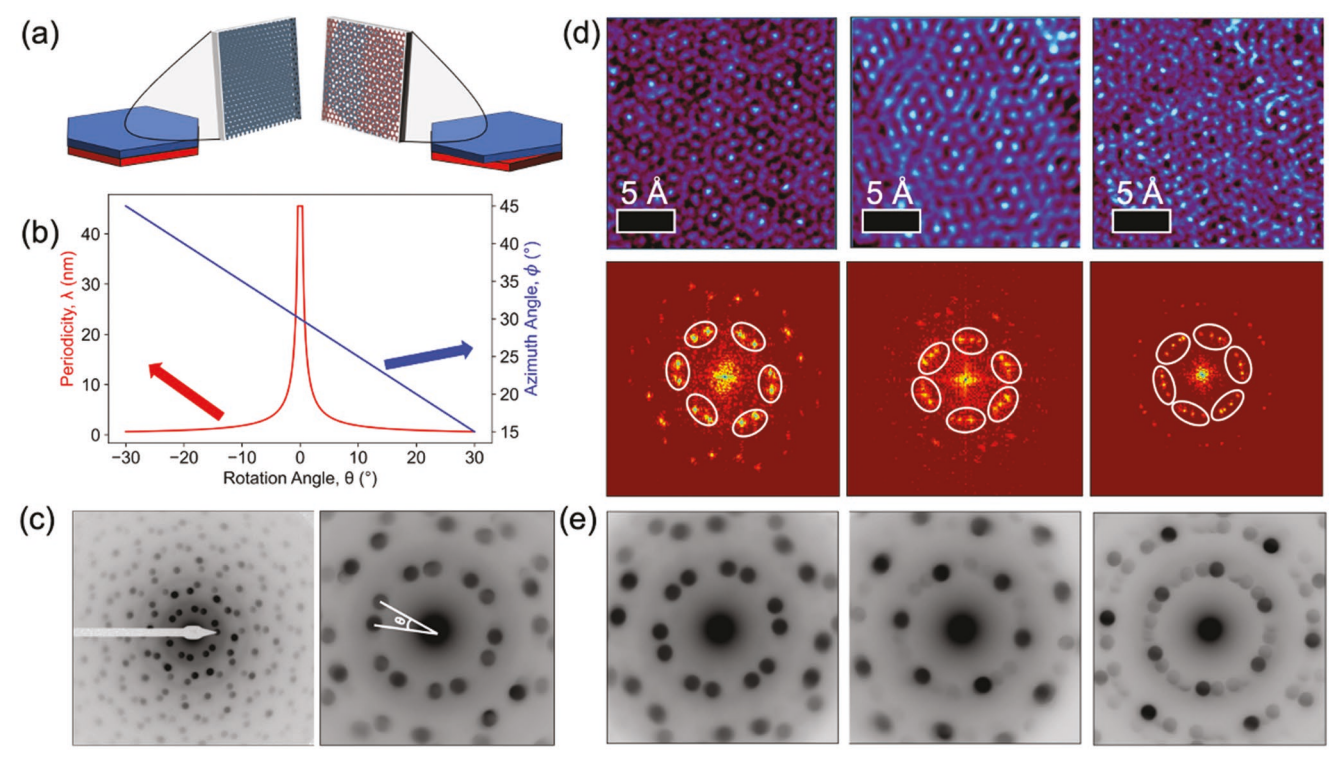


Figure 2. Characterization methodology of moiré patterns in misaligned MoS2. a) 3D atomistic reconstruction of (left) vertically stacked hexagonal lattices with no mismatch and (right) 30° rotationally misaligned hexagonal lattices. b) Superlattice wavelength (red) and moiré angle as a function of the rotational angle between vertically stacked sheets of MoS₂, c) SAED pattern (left) of MoS₂ displaying evidence of rotationally misaligned layers and pseudo sixfold symmetry and (right) high-pixel resolution SAED displaying the approach to calculate θ . d) HRTEM micrographs and corresponding FFTs for the rotational misalignment between 2, 3, and 4 layers of MoS₂, respectively. White circles in FFTs show the coupling of diffraction peaks in the first Brillouin zone. e) SAED patterns of 2, 3, and 4 layers.

between two pristine layers on the left, and a 30° misalignment between two defected layers on the right. The resulting projection is a schematic of the interference pattern produced from the respective hexagonal lattices, representing the origin of moiré patterns in our study. Figure 2b is a plot of the allowed periodic boundary conditions for MoS2 homobilayers, where the periodicity of the pattern (red) and relative rotation of the MoS₂ lattice (blue) are shown with respect to the rotation angle (black). The allowed rotation angles span from −30° to 30°, while the periodicity has a maximum allowable value of ≈42 nm assuming a rotational mismatch of approximately \pm 0.3°. The plot described was constructed based on two equations^[41–45]

$$\lambda = \frac{a_0}{2 \times \sin\left(\frac{|\theta|}{2}\right)} \tag{1}$$

$$\phi = \frac{\pi}{6} - \frac{\theta}{2} \tag{2}$$

where λ is the wavelength of the moiré pattern, α_0 is the lattice constant of MoS_2 , θ is the rotation angle between two sheets of MoS₂, and ϕ is the azimuth angle or the angle of the interference patterns from the resulting moiré fringes.

Figure 2c is a SAED pattern of rotationally misaligned sheets of MoS₂, and from the diffraction pattern, we can visualize the preservation of the pseudo sixfold rotational symmetry at highorder lattice vectors. The SAED pattern on the right displays how the rotational mismatch is calculated in this study, the coupled diffraction peaks in the first Brillouin Zone (BZ) represent two different layers, and the angle between the peaks is how θ is calculated. Figure 2d describes the approach of identifying the number of rotationally misaligned layers, which is broken down into two approaches. First, HR-STEM micrographs are collected with the corresponding fast Fourier transforms (FFTs), where the number of coupled diffraction peaks in the first BZ represents the number of rotationally misaligned layers of MoS₂. One can visualize the contrast difference in the diffraction peaks with respect to one another, owing to the intensity decay of layers embedded in the depths of the material. Accordingly, this opens the possibility to determine the rotational misalignment between surface layers and embedded layers, as layers closer to the surface diffract more strongly from proximity to the electron source. Figure 2e is a sequence of SAED patterns representing a way to distinguish the number of misaligned layers with high precision. In this study, we focus on two misaligned layers of MoS2 as this provides the most accurate insight into the defect-property relationship.

4. The Physics behind Moiré Superlattice **Formation**

Next, we display extended defects induced from irradiation: V_{Mo3S9} , V_{Mo4S18} , V_{Mo9S45} , and V_{Mo8S48} in Figure 3a. In each case,

16136829, 0, Downloaded from https://onlinelibrary.wiley.com/doi/10.1002/smll.202300098 by Oak Ridge National Laboratory, Wiley Online Library on [07/04/2023]. See the Terms and Conditions (https://onlinelibrary.wiley.com/term

-and-conditions) on Wiley Online Library for rules of use; OA articles are governed by the applicable Creative Commons License

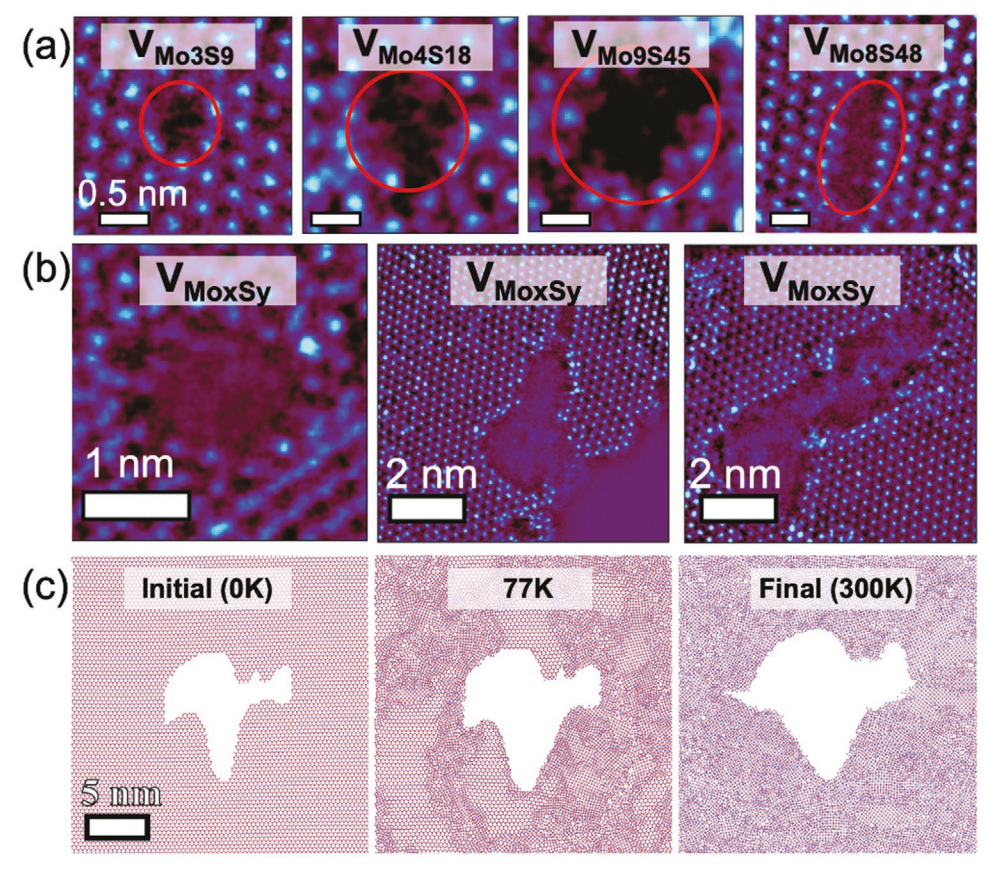


Figure 3. Atomically resolved HAADF-STEM images of extended defect complexes in ion-irradiated sheets of MoS₂. a) Pores found in sheets of MoS₂ post ion irradiation in order of increasing size. All scale bars represent 0.5 nm. b) Larger pores found in sheets of MoS₂ post-ion irradiation in which mapping individual atoms from the lattice became difficult due to the range of the defects. c) Initial, intermediate (77K) and final state of computationally generated nanopore in MD simulations. The final state shows the distribution of damage propagating from the pore as the temperature increases.

dangling bonds are still present around the pores, marking increased susceptibility for extrinsic defects to bind to the edges of these defect sites. In various regions of the sample, irradiation pushes the material away from its equilibrium position near the site of impact. Figure S7, Supporting Information, displays a non-equilibrium lattice from the -180 °C irradiation, which is formed from the nearby presence of disorder. At −180 °C, the isolated intrinsic defects still have a relatively small inter-defect distance without aggregating to form vacancy clusters, which can be attributed to the vacancies not being sufficiently thermally activated during creation. Additionally, at this temperature, vacancy emission is faster than void development. Figure 3b provides examples of some of the largest vacancy complexes post-irradiation. It is already understood that larger complexes induce more impactful deformation fields at further distances from the defects, so we computationally generate nanopores of comparable sizes during our molecular dynamics simulations to quantify the impact of deformation fields on the surrounding lattice, as shown in Figure 3c. Here, we display the initial state of the nanopore, and the final state after the structure relaxes. One can see when generating complex morphological pores, the damage propagates more fiercely in various directions depending on the morphology at each edge.

Figure S8, Supporting Information, displays the rotational misalignment within the periodic boundary conditions of dissimilar hexagonal lattices (as plotted in Figure 2b). In Figure 4, STEM images are shown to assist in probing the local environment with rotation angle and display the periodicity of the lattice versus rotation angle. This is done with the assistance of the FFTs in the inset of each high-resolution STEM image. FFTs displayed to provide a visual of how corresponding moiré superlattices in reciprocal space are used to accurately calculate rotation angles. Arrows point to the region of interest (i.e., defects) that impacts the rotation angle of the grain. In Figure 4a, the STEM images represent misoriented grains in a relatively pristine environment, accounting for the small rotation angle of up to $\approx 8^{\circ}$. In Figure 4b, there is an etched pit in the center of the micrograph where the top layer is missing. This surface-sensitive vacancy cluster induces slight deformations to the surrounding lattice causing an increased rotation angle. In Figure 4c, a unique phase boundary emerges of α | 1T | 2H in a range of \approx 2 nm, which was generated at 800 °C. There is also the possibility for an amorphous phase bordering a crystalline 2H-phase with Mo-rich regions at the interface. In these scenarios, the rotation angle lies in the interval of 20°-26°. Extended defects, that is, vacancy clusters, nanopores, and cracks, generated the largest amount of deformation in the material, as displayed in Figure 4d,e. In Figure 4d, arrows point to nanopores, in which stress emanates from the site of the vacancy cluster. The grains positioned next to the nanopores had the largest misorientation angles observed

Figure 4. Probing varying degrees of lattice disorder with θ where black arrows represent the region of interest. a) Pristine micrographs representing small misorientation angles. b) Disordered micrograph representing a discontinuity in the form of a pore present solely in the top layer. c) Amorphous edges of MoS₂ leading to large misorientation angles at the crystalline boundary. d) Grains adjacent to nanopores to generating large misorientation angles on the edge of the periodic boundary conditions. e) Cracks propagating through a MoS₂ film with a \approx 25° misorientation on neighboring grains. f) A plot of stress in the film, σ , versus θ (red) and ϕ (blue). Colored regions correspond to each subsection detailed from the micrographs in (a–e).

in this study. Finally, Figure 4e shows regions where cracks propagate in a MoS₂ film. These elongated discontinuities also have high-angle moiré structures in the neighboring grains owing to the defect-induced crack blunting. The structural discontinuity at the edges of MoS₂ flakes has been captured in Figure S9, Supporting Information.

As previously stated, nanopores shown in Figure 3a,b emit large deformation fields and result in the formation of moiré superlattices illustrated in Figure 4. Since we used FFTs to calculate components of the deformations response of the material, we briefly introduce the reciprocal space analysis. First, we use κ to represent a reciprocal lattice vector rotated by angle

16136829, 0, Downloaded from https://onlinelibrary.wiley.com/doi/10.1002/smll.202300098 by Oak Ridge National Laboratory, Wiley Online Library on [07/04/2023]. See the Terms and Conditions (https://onlinelibrary.wiley.com/

and-conditions) on Wiley Online Library for rules of use; OA articles are governed by the applicable Creative Commons License

www.small-iournal.com

 θ to yield the relationship of $\kappa' = \hat{R} \times \kappa$. Then to represent our reciprocal lattice vector along the direction of strain, we use the following equation

$$\kappa_0' = \frac{1}{(1 + \varepsilon_0)} \hat{R}(\theta) \times \kappa \tag{3}$$

where ε is the strain in the material. Next, we substitute strain out to facilitate the discussion of stress in the film, using the following correlation of $\varepsilon = \sigma/E$, where E is the modulus of elasticity taken to be 285 GPa. [46,47] To calculate uniaxial stress in the film as a function of rotation angle, we derived the following expression [45]

$$\lambda = \frac{a_0 \left(1 + \frac{\sigma_{xx}}{E} \right)}{2 \sqrt{\left(1 + \frac{\sigma_{xx}}{E} \right) \sin^2 \left(\frac{\theta}{2} \right) + \frac{\sigma_{xx}^2}{4E^2}}} \tag{4}$$

We provide a plot of stress in the film, σ_{xx} , versus θ (red) and ϕ (blue) in Figure 4f. The colored regions in the chart correspond to the lattice environments in which the rotation angles were calculated. Accordingly, increased stress in the film led to larger rotation angles and smaller interference patterns. Figure S10, Supporting Information, is an atomically resolved STEM image depicting misorientation boundaries traversing across the lattice. The white arrow originates from the defect-rich α region with a phase boundary resulting in a 20.5° misorientation, these deformation fields decay with increasing distance from the α region where three misorientations boundaries are shown with yellow dashed lines along the path of the

arrow. Therefore, emphasis is placed on the notion that misorientation angles are non-uniform because deformation fields decay at a rate away from disordered regions in the lattice.

These misorientation boundaries resemble ripples or elastic surface waves. It is therefore not unreasonable to assume that nanopores introduce stresses to the material and excite SAWs, which could be responsible for the observed moiré patterns. Graphene and 2D transition metal dichalcogenides (TMDCs) are highly flexible: they deform easily normal to the 2D plane. Their flexibility can be quantified by the Föppl–Von Karman number, $\gamma = \frac{EA}{\kappa}$, where E is the Young's modulus, k is the bonding modulus, and Δ is the area of the system. The value

bending modulus, and A is the area of the system. The value of γ is high for 2D-MoS₂, and therefore, it deforms and folds easily like a piece of paper. We hypothesize that thermoelastic stresses and strains around nanopores not only deform atomically thin MoS₂ layers normal to the 2D plane but also excite SAWs, which induce relative rotation between the layers to generate moiré patterns seen in our electron microscopy images.

To test this hypothesis, we performed MD simulations and mapped out the time evolution of in-plane and out-of-plane atomic deformations, stress distributions, relative rotations, and moiré patterns in the bilayer at various temperatures. The simulation results validate our hypothesis: out-of-plane atomic deformations, z, and thermoelastic stresses in the bilayer provide direct evidence for SAWs emanating from nanopores. **Figure 5** shows MD results for the bilayer in which the bottom MoS_2 monolayer has a single nanopore of the same size and shape as in our experiment. Figure 5a,b is snapshots of out-of-plane atomic displacements, z, in the bilayer at time t = 30 and 45 ps. Here, the temperature of the system is 77 K. These

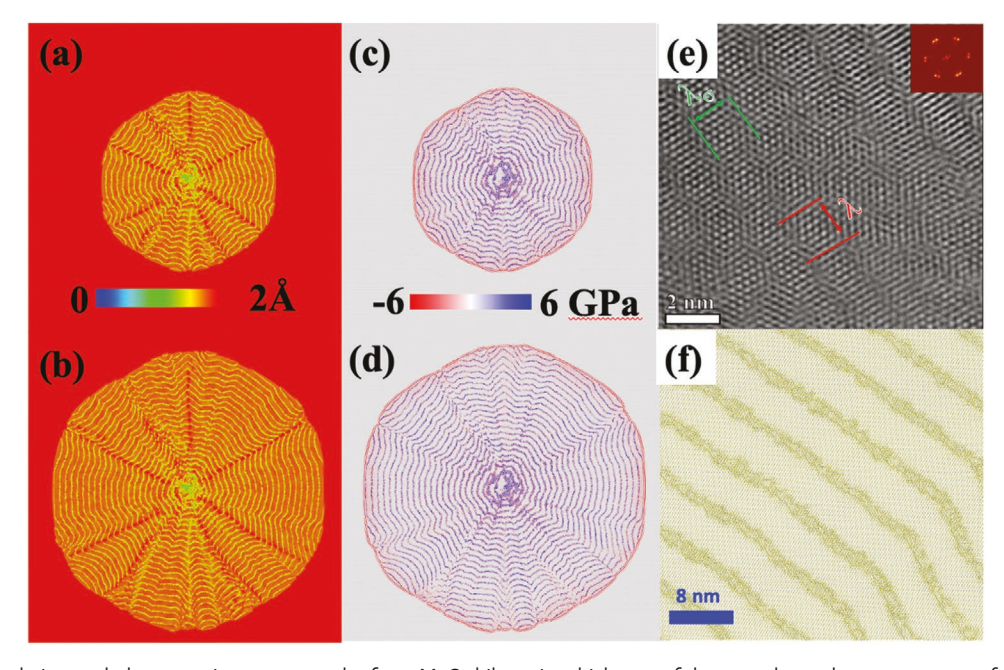


Figure 5. MD simulation and electron microscopy results for a MoS_2 bilayer in which one of the monolayers has a nanopore of the same size and shape as in our experiment. The simulated system size is 300×300 nm², and the system contains 6584217 atoms. The temperature of the system is -196 °C. Panels (a) and (b) are snapshots of out-of-plane displacements at time t=30 and 45 ps, respectively. Panels (c) and (d) show corresponding atomic stress distributions. Panel (e) is an HR-TEM image with an associated FFT pattern insert showing that the traces left behind by the SAW has ordered regions separated by disordered regions. Panel (f) is an MD configuration away from the nanopore. In this snapshot, the disordered region has fivefold and sevenfold coordinated Mo atoms and fourfold coordinated S atoms. The ordered region is the 2H structure.

www.advancedsciencenews.com



16138289, D. Downloaded from https://onlinelibrary.wiley.com/doi/10.1002/smll.202300098 by Oak Ridge National Laboratory, Wiley Online Library on [07/04/2023]. See the Terms and Conditions (https://onlinelibrary.wiley.com/terms-and-conditions) on Wiley Online Library for rules of use; OA articles are governed by the applicable Creative Commons Licenses

www.small-journal.com

panels show a SAW (yellow) originating at the nanopore and propagating through the MoS₂ bilayer (red).

The Supporting Information has movies of SAWs propagating separately on the two monolayers. The SAW originates primarily at the corners of the nanopore where the local stresses are higher than at other points on the nanopore boundary. Figure 5c,d displays average values of the diagonal components of atomic stress distributions at time t=30 and 45 ps. Figure 5a–d indicates that the SAW tends to form a hexagonal pattern as it spreads through the bilayer. From the calculated velocity of the SAW, $c=3.48 \rm \ km\ s^{-1}$, we have computed Young's modulus, Y, using the formula

$$c = \frac{0.87 + 1.12\nu}{1 + \nu} \sqrt{\frac{E}{2\rho(1 + \nu)}}$$
 (5)

where ρ is the mass density and v (= 0.25) is the Poisson's ratio. The calculated Young's modulus of the bilayer with a nanopore is 232 GPa. For a pristine MoS₂ monolayer without the nanopore, the MD simulation gives E=266 GPa and the experimental value is 265 ± 13 GPa, which agrees reasonably well with our experimental calculations.

We have compared experimental electron diffraction patterns with atomic configurations generated by MD simulations. In Figure 5, panels (e) and (f) show an experimental HR-TEM micrograph and an MD configuration of atoms away from the nanopore after the passage of SAW through this region of the bilayer. Both experiment and simulation images show nearly parallel grains of ordered regions separated by disordered grain boundaries. The ordered regions are the 2H phase of MoS₂ and the disordered regions contain defects that are mostly fivefold and sevenfold coordinated Mo and fourfold coordinated S atoms. The simulations also reveal that the SAW propagation induces relative rotation between the S layers, giving rise to moiré patterns that match the ones closely seen in our experiments.

The Supporting Information contains MD results for the bilayer in which the bottom MoS2 layer has multiple nanopores. Upon heating, SAWs originate from each nanopore and propagate through the system with nearly the same velocity. The interference of SAWs produces interesting patterns in displacement and stress profiles. The transfer learning analysis of atomic configurations in the bilayer shows a mixture of 2H and 1T structures and line defects consisting of fivefold and sevenfold coordinated Mo atoms and fourfold coordinated S atoms (Figures S12 and S13, Supporting Information). These types of line defects have been observed in STEM images of MoS₂ bilayers. Transfer learning was employed to supplement MD simulations in this work to compensate for memory issues in the computation. Atom-based analysis of 2H, 1T, and defects uses geometric arguments where it computes the skew between the atoms on one layer with respect to the layer below. This computation uses intensive memory as it is required for every Mo atom to first construct its neighbor list to identify the relative skew. This code cannot be run for large systems serially due to out-of-memory issues as heap space will quickly run out for larger systems. Therefore, we use a CNN which deals with a 10 Å neighborhood around every atom and therefore can scale very efficiently for any arbitrary system size.

Figure S14, Supporting Information, shows the out-of-plane atomic displacement when the wave reaches the edges of the top layer. The pattern changes when the SAW leaves the bilayer and travels only on the bottom monolayer. The edge discontinuities generate wavelets because the edge stresses are highly inhomogeneous, see Figure S12, Supporting Information. The SAW propagation generates pronounced structural changes and interference patterns in the bilayer. In the first few picoseconds of the evolution, the bilayer remains in the 2H phase. However, when the SAW reaches the edges of the top layer, point and line defects are formed in regions of high stress.

In summary, we have shown that the twist angle in vdW solids can be controlled by varying the degree of disorder in the surrounding atomic environment. In homobilayers of MoS₂, generating intrinsic defects causes a lattice mismatch between similar materials, so the layers rotate with respect to one another to minimize the elastic deformation energy. Temperature-controlled ion beam irradiation assisted in engineering various polymorphs and phase boundaries in MoS2, which was attributed to stress fields propagating from regions of high defect concentrations. There was a direct correlation between the degree of disorder and rotation angle, therefore providing a pathway to engineering rotational mismatch within the full periodic boundary conditions of MoS2. Large nanopores were fabricated from the heavy ion irradiation, which generated the most impactful stress fields in this study, leading to the emergence of SAWs laterally across the sheet. While prospective applications for this work are still in their infancy, the objective of this study was to provide a fundamental basis pertaining to why similar materials rotate with respect to one another and non-conventional means to control it. However, the twistronics revolution has gained traction in recent years, and controlling the misorientation angles can change the electronic structure of materials, from engineering insulating and superconducting states, [50] to drastic alterations of the thermal conductivity of the material.^[51] Still, future work is necessary to probe the electronic structure of the moiré patterns with low-loss electron energy loss spectroscopy (EELS) and to analyze the periodic potential of MoS2 charge carriers.

5. Experimental Section

Experimental Methods: Monolayer MoS2 powder was purchased from 2D semiconductors for high crystalline quality and purity of the material. The powder was composed of monolayer flakes that created single-layer sheets in powder form. However, the powder settled in the glass vial, and naturally began to stack in sequence again as vdW force attraction favored this process energetically. To compensate for this, an additional sonication was performed to cleave in between the vdW planes. The powder was submerged in N,N-dimethylformamide (DMF) at a concentration of 15 mg $\,\mathrm{mL^{-1}}$ in a 4 mL glass vial. DMF was sonicated of choice because the similarities of the surface tension between the solvent and MoS2 reduce the energetic barrier to break the vdW forces in between the planes. The sonication lasted for 1.5 h to help separate the flakes based on density. The sonication time chosen was based on shorter intervals of time not providing good interlayer separations of the flakes and longer intervals generating Mo-rich flakes by sputtering S atoms from the lattice. Further details of the fabrication can be found in the previous work.^[52] Finally, the newly dispersed flakes were dropcasted onto holey-carbon TEM grids for analysis.

www.small-journal.com

The in situ TEM irradiation experiments were performed in the I³TEM facility in the Center for Integrated Nanotechnologies (CINT) at Sandia National Laboratories^[53] with a JEOL 2100 TEM with the electron beam blanked to evade additional damage on the specimen. Flakes were irradiated with 2.8 MeV Au⁴⁺ ions at temperatures of -180, 25, 300, and 800 °C, cooled with a Gatan double tilt cryo holder. The irradiation dose rate through all experiments remained constant at 3.95×10^{10} cm⁻² s⁻¹. The calculated fluence was 1×10^{13} cm⁻². During irradiation, the sample was titled 30° relative to the electron beam resulting in the Au ions having an incident angle of 60° relative to the sample normal. STEM experiments were performed on a Nion aberration-corrected UltraSTEM 100 operated at an accelerating voltage of 60 kV. The experiments were performed with a convergence semiangle of 30 mrad. Brightfield HRTEM images and SAED patterns were collected with an FEI Talos F200i at 80 kV. SAED patterns were collected with a 40 μm SA aperture size.

Computational Methods: The equilibrium structures and in-plane displacements for seven types of vacancy defects in monolayer MoS_2 were computed using DFT as implemented in the Vienna ab initio simulation package (VASP). [54] Calculations were performed using projector-augmented wave pseudopotentials, [55,56] treating the exchange-correlation using the Perdew–Burke–Ernzerhof[57] generalized gradient approximation functional. A plane-wave cutoff energy of 520 eV for the plane-wave basis set, Methfessel–Paxton smearing [58] with a smearing energy width of 0.10 eV, and a 3×3 Γ -centered Monkhorst–Pack k-point mesh [59] for the Brillion-zone integration were employed. Each vacancy or vacancy cluster was created within a 5×5 supercell with 20 Å vacuum spacing between periodic layers and allowed to relax until forces were less than 10 meV Å $^{-1}$.

MD simulations were performed to gain physical insight into experimental observations of defect-driven moiré patterns in MoS_2 bilayers. The MD simulations were based on an SW-type forcefield which consisted of two- and three-body terms. The forcefield was validated by first-principles quantum simulations and experimental data on thermomechanical properties and phonon dispersions of $2D\text{-}MoS_2$ under ambient conditions, as well as under tensile and compressive loadings. The forcefield development and validation are described in the previous $\text{work}^{[60-62]}$ and Supporting Information. The phonon dispersion curves can be found in Figure S11, Supporting Information.

MD simulations were performed with the SW potential for many different sizes of MoS_2 bilayers. Here, two sets of simulation results for bilayers of dimensions 300×300 nm² were presented. In the first set, the bottom monolayer had a single nanopore of the same size (diameter ≈ 10 nm) and shape as in the experiment. In the second set of simulations, the bottom monolayer had a random distribution of smaller pores. Pristine monolayers of MoS_2 were placed above those with nanopores. The initial separation between the two monolayers was 4.8 Å, which corresponded to the distance where the interaction between the monolayers was minimum. The bilayers were relaxed with the conjugate gradient minimization scheme and heated to experimental temperatures (–196 and 27 °C) in the NVT ensemble. Each system was equilibrated for 250 ps and then structural, dynamical, and thermomechanical properties were computed over 250 ps.

The bilayers underwent interesting structural, dynamical, thermal, and mechanical changes. Machine learning (ML) was used to delineate 2H and 1T phases and identify defects in the MD simulation data. The ML approach $^{[63]}$ was based on a convolutional neural network (CNN) $^{[64]}$ and involved transfer learning because a CNN trained on a prior data set consisting of MD configurations of crack propagation in a MoSe2 monolayer was used. That data set featured 2H and 1T structures, as well as line defects at 2H and 1T interfaces. Here, only a small fraction of MD configurations (~5%) of MoS2 was used to augment the training of the CNN. The rest of the MD data was used for testing CNN against the ground-truth MD analysis of 2H and 1T phases and defects in MoS2 bilayers. The architecture and the training, validation, and testing of CNN are presented in Supporting Information. The source code for the training is freely available on Zenobo at: https://zenodo.org/record/7423346#.YSfn]S-B1Z0.

Supporting Information

Supporting Information is available from the Wiley Online Library or from the author.

Acknowledgements

This work was supported by the US Department of Energy, Office of Science, Basic Energy Sciences, under Award #DESC0019014 "Establishing defect-property relationships for 2D nanomaterials." This work was performed, in part, at the Center for Integrated Nanotechnologies, an Office of Science User Facility operated by the US Department of Energy (DOE) Office of Science. Sandia National Laboratories is a multimission laboratory managed and operated by National Technology & Engineering Solutions of Sandia, LLC, a wholly-owned subsidiary of Honeywell International, Inc., for the US DOE's National Nuclear Security Administration under contract DE-NA-0003525. The views expressed in the article do not necessarily represent the views of the US DOE or the United States Government. A portion of this research was conducted at the Center for Nanophase Materials Sciences, which is a DOE Office of Science User Facility. R.K. and A.N. would like to acknowledge the support of the National Science Foundation, Future Manufacturing Program, Award 2036359. R.G.H. and A.M.Z.T. would like to acknowledge the support of the National Science Foundation under Awards No. 1748464 and No. 1539916. This research used computational resources provided by the University of Florida Research Computing Center. [65]

Conflict of Interest

The authors declare no conflict of interest.

Data Availability Statement

The data that support the findings of this study are available in the supplementary material of this article.

Keywords

2D materials, defects, moiré patterns, surface acoustic waves

Received: January 4, 2023 Revised: March 6, 2023 Published online:

- A. A. Arnold, T. Shi, I. Jovanovic, S. Das, ACS Appl. Mater. Interfaces 2019, 11, 8391.
- [2] Z. Li, F. Chen, Appl. Phys. Rev. 2017, 4, 011103.
- [3] T. Ohta, J. T. Robinson, P. J. Feibelman, A. Bostwick, E. Rotenberg, T. E. Beechem, *Phys. Rev. Lett.* 2012, 109, 186807.
- [4] M. Liao, Z. Wei, L. Du, Q. Wang, J. Tang, H. Yu, F. Wu, J. Zhao, X. Xu, B. Han, K. Liu, P. Gao, T. Polcar, Z. Sun, D. Shi, R. Yang, G. Zhang, Nat. Commun. 2020, 11, 2153.
- [5] C. Jin, E. C. Regan, A. Yan, M. I. B. Utama, D. Wang, S. Zhao, Y. Qin, S. Yang, Z. Zheng, S. Shi, K. Watanabe, T. Taniguchi, S. Tongay, A. Zettl, F. Wang, *Nature* 2019, 567, 76.
- [6] Y. Cao, V. Fatemi, S. Fang, K. Watanabe, T. Taniguchi, E. Kaxiras, P. Jarillo-Herrero, *Nature* 2018, 556, 43.
- [7] A. J. Mannix, A. Ye, S. H. Sung, A. Ray, F. Mujid, C. Park, M. Lee, J.-H. Kang, R. Shreiner, A. A. High, D. A. Muller, R. Hovden, J. Park, Nat. Nanotechnol. 2022, 17, 361.

www.advancedsciencenews.com

- P. Majchrzak, Z. Jiang, D. Biswas, P. Dubin, J. Avila, K. Watanabe,
- P. M. Ajayan, *Nano Lett.* 2011, 11, 2032.
 W. Yang, G. Chen, Z. Shi, C.-C. Liu, L. Zhang, G. Xie, M. Cheng,
 D. Wang, R. Yang, D. Shi, K. Watanabe, T. Taniguchi, Y. Yao,
 Y. Zhang, G. Zhang, *Nat. Mater.* 2013, 12, 792.

[8] Z. Liu, L. Song, S. Zhao, J. Huang, L. Ma, J. Zhang, J. Lou,

- [10] Y. Shi, W. Zhou, A.-Y. Lu, W. Fang, Y.-H. Lee, A. L. Hsu, S. M. Kim, K. K. Kim, H. Y. Yang, L.-J. Li, J.-C. Idrobo, J. Kong, *Nano Lett.* 2012, 12, 2784
- [11] G. Gao, W. Gao, E. Cannuccia, J. Taha-Tijerina, L. Balicas, A. Mathkar, T. N. Narayanan, Z. Liu, B. K. Gupta, J. Peng, Y. Yin, A. Rubio, P. M. Ajayan, Nano Lett. 2012, 12, 3518.
- [12] L. Du, H. Yu, M. Liao, S. Wang, L. Xie, X. Lu, J. Zhu, N. Li, C. Shen, P. Chen, R. Yang, D. Shi, G. Zhang, Appl. Phys. Lett. 2017, 111, 263106
- [13] R. Rebeiro-Palau, C. Zhang, K. Watanabe, T. Taniguchi, J. Hone, C. R. Dean, Science 2018, 362, 690.
- [14] Z. Zhang, X. Yang, K. Liu, R. Wang, Adv. Sci. 2022, 9, 2105201.
- [15] Y. Zhu, Y. Sun, H. Zhang, Y. He, W. Liu, R. Wang, Nano Res. 2022, 15, 8493
- [16] A. Shan, X. Teng, Y. Zhang, P. Zhang, Y. Xu, C. Liu, H. Li, H. Ye, R. Wang, Nano Energy 2022, 94, 106913.
- [17] Z. Yan, X. Li, Y. Li, C. Jia, N. Xin, P. Li, L. Meng, M. Zhang, L. Chen, J. Yang, R. Wang, X. Guo, Sci. Adv. 2022, 8, eabm3541.
- [18] H. Ye, F. Yang, Y. Sun, R. Wang, Small Methods 2022, 6, 2200171.
- [19] T. Huang, P. Han, X. Wang, J. Ye, W. Sun, S. Feng, Y. Zhang, J. Phys. D: Appl. Phys. 2017, 50, 114005.
- [20] E. Preciado, F. J. R. Schülein, A. E. Nguyen, D. Barroso, M. Isarraraz, G. von Son, I.-H. Lu, W. Michailow, B. Möller, V. Klee, J. Mann, A. Wixforth, L. Bartels, H. J. Krenner, Nat. Commun. 2015, 6, 8593.
- [21] A. Hernández-Mínguez, Y.-T. Liou, P. V. Santos, J. Phys. D: Appl. Phys. 2018, 51, 383001.
- [22] K. Burns, A. M. Z. Tan, H. GordonV, T. Wang, A. Gabriel, L. Shao, R. G. Hennig, A. Aitkaliyeva, *Phys. Rev. B* 2020, 102, 085421.
- [23] K. Burns, A. M. Z. Tan, A. Gabriel, L. Shao, R. G. Hennig, A. Aitkaliyeva, J. Mater. Res. 2020, 35, 949.
- [24] M. L. Ster, T. Maerkl, P. J. Kowalczyk, S. A. Brown, Phys. Rev. B 2019, 99, 075422.
- [25] S. Yang, Y. Chen, C. Jiang, InfoMat 2021, 3, 397.
- [26] A. Apte, V. Kochat, P. Rajak, A. Krishnamoorthy, P. Manimunda, J. A. Hachtel, J. C. Idrobo, S. A. S. Amanulla, P. Vashishta, A. Nakano, R. K. Kalia, C. S. Tiwary, P. M. Ajayan, ACS Nano 2018, 12, 3468.
- [27] S. Susarla, P. Manimunda, Y. M. Jaques, J. A. Hachtel, J. C. Idrobo, S. A. S. Amnulla, D. S. Galvão, C. S. Tiwary, P. M. Ajayan, ACS Nano 2018, 12, 4036.
- [28] P. Manimunda, Y. Nakanishi, Y. M. Jaques, S. Susarla, C. F. Woellner, S. Bhowmick, S. A. S. Asif, D. S. Galvão, C. S. Tiwary, P. M. Ajayan, 2D Mater. 2017, 4, 045005.
- [29] W. Li, X. Wang, X. Zhang, S. Zhao, H. Duan, J. Xue, Sci. Rep. 2015, 5, 9935.
- [30] E. Glushkov, M. Macha, E. Räth, V. Navikas, N. Ronceray, C. Y. Cheon, A. Ahmed, A. Avsar, K. Watanabe, T. Taniguchi, I. Shorubalko, A. Kis, G. Fantner, A. Radenovis, ACS Nano 2022, 16, 3695
- [31] S. Bertolazzi, S. Bonacchi, G. Nan, A. Pershin, D. Beljonne, P. Samorì, Adv. Mater. 2017, 29, 1606760.
- [32] K. Yin, S. Huang, X. Chen, X. Wang, J. Kong, Y. Chen, J. Xue, ACS Appl. Mater. Interfaces 2018, 10, 28909.
- [33] A. Krasheninnikov, K. Nordlund, Nucl. Instrum. Methods Phys. Res., Sect. B. 2004, 216, 355.
- [34] M. Kapfer, B. S. Jessen, M. E. Eisele, M. Fu, D. R. Danielsen, T. P. Darlington, S. L. More, N. R. Finney, A. Marchese, V. Hsieh,

- P. Majchrzak, Z. Jiang, D. Biswas, P. Dubin, J. Avila, K. Watanabe, T. Tanihuchi, S. Ulstrup, P. BØggild, P. J. Schuck, D. N. Basov, J. Hone, C. R. Dean, *ArXiv* **2022**, *2209*, 10696.
- [35] L. Huder, A. Artaud, T. L. Quang, G. Tramble de Laissardière, A. G. M. Jansen, G. Lapertot, C. Chapelier, V. T. Renard, Phys. Rev. Lett. 2019, 120, 156405.
- [36] W. Zhou, X. Zou, S. Najmaei, Z. Liu, Y. Shi, J. Kong, J. Lou, P. M. Ajayan, B. I. Yakobson, J.-C. Idrobo, *Nano Lett.* 2013, 13, 2615.
- [37] J. F. Ziegler, M. D. Ziegler, J. P. Biersack, Nucl. Instrum. Methods Phys. Res., Sect. B 2010, 11-12, 1818.
- [38] J. Hong, Z. Hu, M. Probert, K. Li, D. Lv, X. Yang, L. Gu, N. Mao, Q. Feng, L. Xie, J. Zhang, D. Wu, Z. Zhang, C. Jin, W. Ji, X. Zhang, J. Yuan, Z. Zhang, *Nat. Commun.* 2015, 6, 6293.
- [39] J. Strachan, A. F. Masters, T. Maschmeyer, ACS Appl. Energy Mater. 2021, 4, 7405.
- [40] Q. Tang, D. Jiang, Chem. Mater. 2015, 27, 3743.
- [41] J. H. Kim, K. Kim, Z. Lee, Sci. Rep. 2015, 5, 12508.
- [42] M. Yankowitz, J. Xue, D. Cormode, J. D. Sanchez-Yamagishi, K. Watanabe, T. Taniguchi, P. Jarillo-Herrero, P. Jacquod, B. J. LeRoy, *Nat. Phys.* 2012, 8, 382.
- [43] Y. Liao, W. Cao, J. W. Connell, Z. Chen, Y. Lin, Sci. Rep. 2016, 6, 26084.
- [44] O. S. Ovchinnikov, A. O'Hara, R. J. T. Nicholl, J. A. Hachtel, K. Bolotin, A. Lupini, S. Jesse, A. P. Baddorf, S. V. Kalinin, A. Y. Borisevich, 2D Mater. 2018, 5, 041008.
- [45] D. L. Miller, K. D. Kubista, G. M. Rutter, M. Ruan, W. A. de Heer, P. N. First, J. A. Stroscio, *Phys. Rev. B* 2010, 81, 125427.
- [46] S. Bertolazzi, J. Brivio, A. Kis, ACS Nano 2011, 5, 9703.
- [47] A. Castellanos-Gomez, M. Poot, G. A. Steel, H. S. J. van der Zant, N. Agraït, G. Rubio-Bollinger, Adv. Mater. 2012, 24, 772.
- [48] A. Föppl, Vorlesungen uber technische Mechanik (Ed: B.G. Teubner), Bd. 5, Aufl, Leipzig, Germany 1907; p. 132.
- [49] T. von Karman, Festigkeitsproblem im Maschinenbau. Encyk. D. Math. Wiss. IV, 1910, 311–385.
- [50] E. Codecio, Q. Wang, R. Koester, S. Che, H. Tian, R. Lv, S. Tran, K. Watanabe, T. Taniguchi, C. N. Lau, Sci. Adv. 2014, 5, eaaw9770.
- [51] M.-L. Lin, Q.-H. Tan, J.-B. Wu, X.-S. Chen, J.-H. Wang, Y.-H. Pan, X. Zhang, X. Chong, J. Zhang, W. Ji, P.-A. Hu, K.-H. Liu, P.-H. Tan, ACS Nano 2018, 12, 8770.
- [52] K. Burns, B. Bischoff, C. M. Barr, K. Hattar, A. Aitkaliyeva, Nanotechnology 2022, 33, 085601.
- [53] K. Hattar, D. C. Bufford, D. L. Buller, Nucl. Instrum. Methods Phys. Res., Sect. B 2014, 338, 56.
- [54] G. Kresse, J. Furthmüller, Phys. Rev. B 1996, 54, 11169.
- [55] P. E. Blöchl, Phys. Rev. B 1994, 50, 17953.
- [56] G. Kresse, D. Joubert, Phys. Rev. B 1999, 59, 1758.
- [57] J. P. Perdew, K. Burke, M. Ernzerhof, Phys. Rev. Lett. 1996, 77, 3865.
- [58] M. Methfessel, A. T. Paxton, Phys. Rev. B 1989, 40, 3616.
- [59] H. J. Monkhorst, J. D. Pack, Phys. Rev. B 1976, 13, 5188.
- [60] A. Krishnamoorthy, A. Mishra, D. Kamal, S. Hong, K.-i. Nomura, S. Tiwari, A. Nakano, R. Kalia, R. Ramprasad, P. Vashishta, SoftwareX 2021, 13, 100663.
- [61] A. Krishnamoorthy, A. Mishra, N. Graber, N. Baradwaj, R. K. Kalia, A. Nakano, P. Vashishta, Comp. Phys. Commun. 2020, 254, 107337.
- [62] A. Mishra, S. Hong, P. Rajak, C. Sheng, K.-i. Nomura, R. K. Kalia, A. Nakano, P. Vashishta, npj Comput. Mater. 2018, 4, 42.
- [63] P. Rajak, A. Krishnamoorthy, A. Mishra, R. Kalia, A. Nakano, P. Vashishta, npj Comput. Mater. 2021, 7, 108.
- [64] P. Rajak, A. Krishnamoorthy, A. Nakano, P. Vashishta, R. Kalia, Phys. Rev. B 2019, 100, 014108.
- [65] https://www.rc.ufl.edu/ (accessed: July 2022).

16138289, D. Downloaded from https://onlinelibrary.wiley.com/doi/10.1002/smll.202300098 by Oak Ridge National Laboratory, Wiley Online Library on [07/04/2023]. See the Terms and Conditions (https://onlinelibrary.wiley.com/terms-and-conditions) on Wiley Online Library for rules of use; OA articles are governed by the applicable Creative Commons Licenses